Editors' Suggestion Featured in Physics

Morphological Attractors in Natural Convective Dissolution

Jinzi Mac Huang [*]
NYU-ECNU Institute of Physics and Institute of Mathematical Sciences, New York University Shanghai, Shanghai 200122, China
and Applied Math Lab, Courant Institute, New York University, New York, New York 10012, USA

Nicholas J. Moore [†]
Mathematics Department, United States Naval Academy, Annapolis, Maryland 21402, USA

(Received 6 September 2021; accepted 1 December 2021; published 11 January 2022)

Recent experiments demonstrate how a soluble body placed in a fluid spontaneously forms a dissolution pinnacle—a slender, upward pointing shape that resembles naturally occurring karst pinnacles found in stone forests. This unique shape results from the interplay between interface motion and the natural convective flows driven by the descent of relatively heavy solute. Previous investigations suggest these structures to be associated with shock formation in the underlying evolution equations, with the regularizing Gibbs-Thomson effect required for finite tip curvature. Here, we find a class of exact solutions that act as attractors for the shape dynamics in two and three dimensions. Intriguingly, the solutions exhibit large but finite tip curvature without any regularization, and they agree remarkably well with experimental measurements. The relationship between the dimensions of the initial shape and the final state of dissolution may offer a principle for estimating the age and environmental conditions of geological structures.

DOI: 10.1103/PhysRevLett.128.024501

Ever-changing geological features on this planet never fail to capture our imagination and inspire new scientific advances. Often, striking features appear when fluid and solid interact, ranging from centimeter scale pebble stones [1,2] to the kilometer scale karst terrains [3,4]. Even planetary-scale plate tectonics are believed to have such a fluid-structure interaction origin [5–8].

The direct study of geophysical structures presents unique challenges owing to the vast range of scales, along with the limitation of only seeing the current state. On the other hand, laboratory-scale experiments combined with judicious physical models have proven valuable in explaining certain formations [9,10], like the growth of icicles [11], river meandering [12–14], the formation of stalactites and stalagmites [15–17], meteor ablation [18], and plate tectonics [5–8]. In this Letter, we investigate one such geomorphological problem, namely, the formation of karst pinnacles [3,19]. We will demonstrate the unusual shape dynamics that result in convergence to a morphological attractor.

Commonly seen in South Asia and the island of Madagascar [20,21], Fig. 1(a) shows the typical shape of the karst pinnacles that comprise stone forests. While their origins remain unclear, studies have related such pinnacles to the dissolution process [4,19,22], as many of these rocks were once immersed under water, and the rock material is slightly water soluble. Two questions naturally arise: How does the rock evolve into individual pinnacles? Why does each pinnacle exhibit the common feature of a sharp apex?

Aimed at addressing such questions, recent experiments employed lab-scale soluble objects to recreate the stone forests purely from the perspective of dissolution and fluid dynamics [23]. These experiments show stone forests to manifest from a single porous, soluble block, highlighting the sharpening of each karst pinnacle as the key to such formations. In these and other [24] experiments, no external flow is imposed, rather the transport of relatively heavy solute sustains a natural convective flow that drives shape evolution.

Huang *et al.* and Pegler and Wykes proposed a boundary-layer based model capable of predicting sharpening [23,25]. Notably, the model reduces to a single integro-PDE that governs shape evolution, denoted here as the sharpening equation (SE). Initial numerical evidence and scaling analysis of the SE suggested shock formation and finite-time blowup of the tip curvature [23]. Likewise, similarity solutions of a matched-asymptotic approximation predict unbounded growth of tip curvature for certain initial conditions [25,26].

Figure 1 shows experimental images of dissolving planar and axisymmetric bodies (see Ref. [23] for experimental details). Measurements of the tip curvature indeed increase over time, as seen in Figs. 1(b) and 1(c), but interestingly give no clear indication of singular behavior. To reconcile these observations, previous studies appealed to the thermodynamic Gibbs-Thomson (GT) effect [27,28], which regularizes the SE and limits the curvature growth.

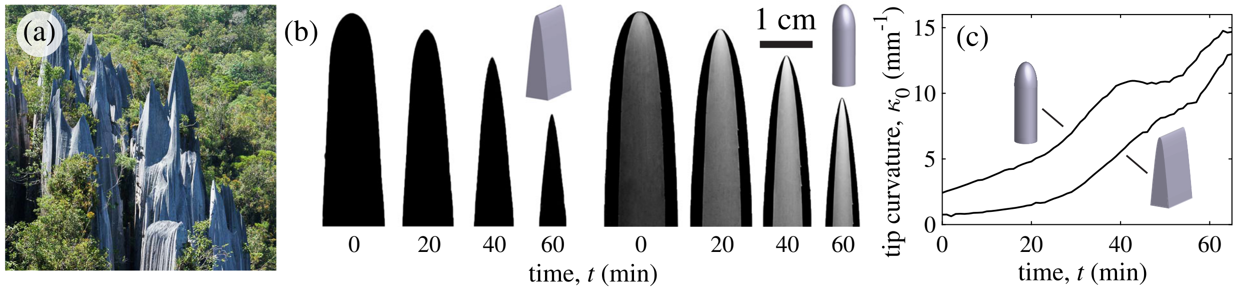

FIG. 1. Dissolution-induced sharpening. (a) Limestone structures form the stone forests of Borneo (Grant Dixon). (b)–(c) Dissolution of lab-scale planar and axisymmetric objects unveils the sharpening process; images from the same set of experiments reported in Ref. [23]. The observed noise in the curvature measurements results from surface impurities, like bubbles, affecting image tracking. The final radius of curvature at the tip was measured to be 60 μm.

However, the strength of the GT term used in previous simulations was at the high end of the range estimated from physical considerations (1–10 μm) [23], thus calling into question whether this term accurately modeled a physical effect or was simply acting to regularize the numerics. For context, the experiments shown in Fig. 1 reach a final tip radius of 60 μm, suggesting that the GT effect is secondary. As such, fundamental questions remain: Does the SE support geometric shock formation? Is there a blowup in tip curvature, and, if so, is the blowup only limited in practice by microscale thermodynamics?

Here, we resolve these and other questions by finding a class of exact solutions to the SE in two and three dimensions that serve as attractors for the shape dynamics. The solutions exhibit large, but finite, tip curvature, indicating that the GT effect is not needed to regularize sharpening. Improved numerical methods, specially tailored to the hyperbolic nature of the SE, show how initially convergent characteristics bend to avoid crossing and eventually straighten in pursuit of the attracting morphology. Revisited experiments confirm the convergence to these exact solutions, thus raising the possibility of using the solutions to infer properties of natural structures.

The model.—In accordance with Fick's law, a soluble interface retreats with normal velocity proportional to the gradient of the solute field $V_n \propto \nabla c \cdot \mathbf{n}$ [2,29,30]. These dynamics can be greatly complicated by the presence of a fluid flow, which significantly distorts the field c and alters local gradients. The flow may be forced externally [1,31–37] or driven by buoyancy variations [23,24,38], as in the present study. The evolution of flow, solute, and body shape are thus inextricably linked.

Because of the large Schmidt and Grashof numbers ($\mathrm{Sc} \sim 10^3$ and $\mathrm{Gr} \sim 10^9$, see Supplemental Material [39]) of the pinnacle experiments, these convective flows are confined to narrow boundary layers, enabling an explicit expression for the 2D interface velocity [23,40]:

$$V_n = -a \cos^{\frac{1}{3}}\theta \left(\int_0^s \cos^{\frac{1}{3}}\theta ds' \right)^{-\frac{1}{4}} \tag{1}$$

where the surface tangent angle $\theta = \theta(s,t)$ is parameterized by the arclength s from the apex, as illustrated in Fig. 2(c). The constant $a \approx 10^{-7}$ m$^{5/4}$/s contains all material and fluid properties. For simplicity, we focus on the 2D case in this Letter, with analogous analysis for axiysymmetric (3D) objects available in the Supplemental Material [39].

The θ-L formulation [30,41–43] offers a single, *scalar* equation that fully describes shape evolution:

$$\frac{\partial \theta}{\partial t} = \frac{\partial V_n}{\partial s} + V_s \frac{\partial \theta}{\partial s}. \tag{2}$$

As above, θ represents the surface tangent angle, and the Cartesian coordinates can easily be recovered from $(d/ds)(x,y) = (\sin\theta, \cos\theta)$. The artificial tangential

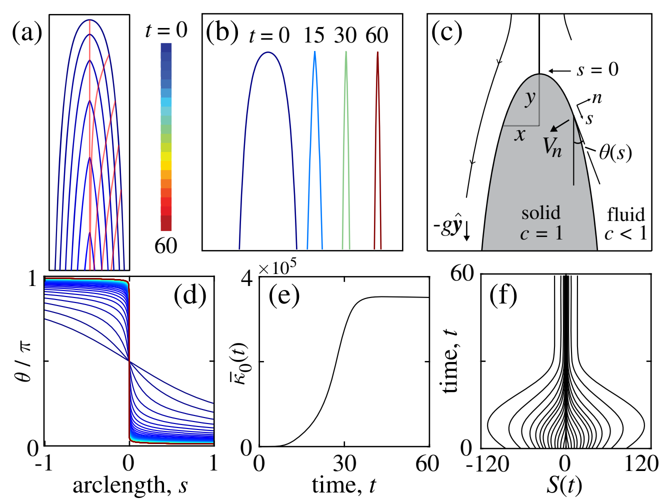

FIG. 2. Simulating dissolution-induced sharpening. (a) Evolution of the initial shape $\theta = \operatorname{arccot} s/\ell$ in two dimensions. (b) Zooming in near the apex illustrates the strong sharpening effect. (c) Model schematic. (d) Profiles of the tangent-angle $\theta(s,t)$ show a steep gradient develop near the apex, $s = 0$, consistent with (e) a tip curvature that increases by 5 orders of magnitude. (f) Characteristic curves show contours of constant θ, with the physical trajectories shown in (a) with red.

velocity $V_s = \int_0^s V_n \partial_s \theta ds'$ enforces an invariant metric with respect to arclength, thereby separating s and t as *independent* variables. Equation (2) with interface velocity Eq. (1) is the nonlinear integro-PDE proposed in Ref. [23], here called the sharpening equation (SE); see Ref. [25] for the Cartesian counterpart.

Previous investigations employed a finite-difference scheme to solve Eq. (2), but with the GT regularization required to maintain numerical stability [23]. Other studies employed a matched-asymptotic expansion, but with approximation error that may grow large with time [25,26]. In contrast, we introduce a method to directly propagate characteristics of Eq. (2), with no regularization and no additional model approximation made.

To that end, consider a location $s = S^{(0)}$ on the initial geometry, with tangent angle $\Theta^{(0)} = \theta(S^{(0)}, 0)$. The trajectory $S(t)$ evolves via the ODE:

$$\dot{S}(t) = \left(R \frac{\partial V_n}{\partial s} - V_s \right) \bigg|_{s=S(t)}, \qquad S(0) = S^{(0)}, \quad (3)$$

where $R = -(\partial\theta/\partial s)^{-1} = \kappa^{-1}$ is the radius of curvature. Combining Eqs. (2) and (3) shows that the tangent angle remains constant along such a *characteristic*, $\theta(S(t), t) = \Theta^{(0)}$, thus providing an implicit solution for any initial profile $\Theta^{(0)} = \theta(S^{(0)}, 0)$. This is the essence of the method of characteristics.

A PDE-based interpretation of Eq. (3) is also possible via implicit functions. That is, regard $s = s(\theta, t)$, where $\theta \in (0, \pi)$ is now the independent variable, to obtain

$$\frac{\partial s}{\partial t} = -\frac{\partial V_n}{\partial \theta} - V_s, \quad (4)$$

$$V_n = -a \cos^{\frac{1}{3}}\theta \left(\int_\theta^{\pi/2} R(\theta', t) \cos^{\frac{1}{3}}\theta' d\theta' \right)^{-\frac{1}{4}}, \quad (5)$$

where now $R(\theta, t) = -\partial s/\partial\theta$ and $V_s = \int_{\pi/2}^{\theta} V_n(\theta') d\theta'$. Crucially, the reformulation in terms of θ implies increased numerical tip resolution in proportion to the sharpening. We thus solve Eqs. (4) and (5) numerically (see the Supplemental Material [39] for implementation details) for a class of left-right symmetric initial conditions.

Results.—As a first numerical test, we simulate the dissolution of the initial profile $\theta(s, 0) = \mathrm{arccot}(s/\ell)$, with $\ell = 1$ and $a = 1$ (for other values, time could be rescaled by the factor $\ell^{5/4}/a$). As seen in Fig. 2(a), dissolution causes the apex to sharpen as the body retreats downwards and diminishes in size. Figure 2(b) shows a few representative shapes at different stages of dissolution, illustrating the dramatic sharpening effect. Figure 2(d) shows the corresponding distributions of the tangent angle, $\theta(s, t)$. Here, a rapid change of tangent angle develops at the tip, as is consistent with the increasing curvature $\kappa = -\partial\theta/\partial s$ there. Indeed, the rescaled tip curvature $\bar{\kappa}_0(t) = \kappa_0(t)/\kappa_0(0)$ shown in Fig. 2(e) increases by 5 orders of magnitude before saturating.

Figure 2(f) shows the characteristic curves $[t, S(t)]$ corresponding to different constant values of the tangent angle $\theta = \Theta^{(0)}$ [the physical trajectories of these curves are shown in red in Fig. 2(a)]. Near the tip ($S \approx 0$) characteristics initially converge towards one another, implying a large range of tangent angles crowded into a small region, i.e., sharpening. Previous discretizations of Eq. (2) interpreted this convergence as a *crossing* of characteristics and thus the formation of a geometric shock. The reformulated Eq. (4), however, reveals that characteristics bend away from one another before ever crossing, thus preventing a finite-time blowup of curvature. Characteristics farther from the tip are seen to change their direction of travel, initially propagating outwards, and then inwards, before they ultimately straighten and travel vertically. At late times, all characteristics are seen to travel vertically, suggesting that a terminal shape has arrived.

Exact solutions.—To examine the possibility of a terminal shape, we take a θ derivative of Eq. (4) to obtain an evolution equation for the radius of curvature [9,44]:

$$\frac{\partial R}{\partial t} = V_n + \frac{\partial^2 V_n}{\partial \theta^2}. \quad (6)$$

Clearly, a steady state of Eq. (6) is given by

$$V_n = -V_0 \sin\theta \quad (7)$$

for any constant V_0, which is the recessional rate of the tip. Equation (7) represents steady translation of a fixed shape. It is the only steady-state V_n that satisfies left-right symmetry. Inserting Eq. (7) into Eq. (5) and inverting gives the equilibrium distribution of R,

$$\frac{R^*}{R_0^*} = \frac{1 + 2\cos^2\theta}{\sin^5\theta}. \quad (8)$$

This class of equilibrium solutions has one degree of freedom R_0^*, which is the equilibrium radius of curvature at the tip. Exact expressions for the Cartesian coordinates of this surface, along with solutions for the corresponding axisymmetric (3D) problem, are given in the Supplemental Material [39]. Though differences exist in the θ-L formulation of the 2D and 3D problems, the final equilibrium solutions are identical when written in Cartesian coordinates.

To test the convergence to this final shape, Fig. 3(a) shows the simulated interfaces from the previous example, but shifted to have the same apex. As seen here and in the close-up, the interfaces indeed collapse to a single profile at late times. Figure 3(b) shows that the corresponding distributions of rescaled curvature radius, $R(\theta, t)/R_0(t)$, converge to the equilibrium shape Eq. (8).

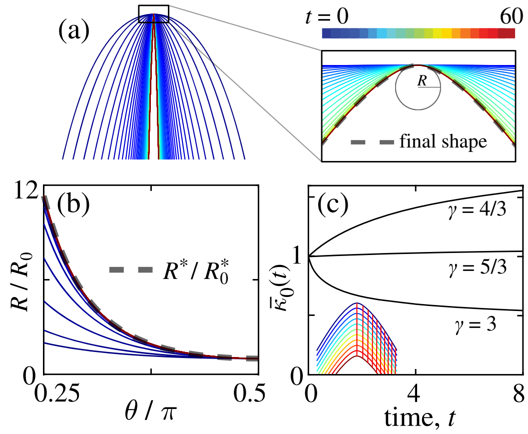

FIG. 3. Convergence towards the equilibrium morphology. (a) Left: Overlaying interfaces in Fig. 2(a) shows a common shape to emerge at late times. Right: Zooming-in near the apex further reveals the convergence towards an equilibrium. (b) The rescaled radius of curvature R/R_0 tends to the exact distribution predicted by Eq. (8). (c) Choosing initial shapes near the equilibrium can lead to sharpening or blunting, as predicted by Eq. (10). Inset: physical shape evolution of the case $\gamma = 5/3$ reveals straight characteristic paths.

Having observed the convergence to the predicted morphology, several questions remain: What happens for different initial conditions? What determines the final tip radius $R_0^* = \lim_{t\to\infty} R(0,t)$? And how can the results be reconciled with previous infinite-curvature predictions [23,26]? To address these questions, we consider a local expansion in small $w = \cos\theta$:

$$s(w,t) = a_1(t)w + a_3(t)w^3 + \ldots, \tag{9}$$

where odd-symmetry has been used. Thanks to the change of variables, V_n can be calculated exactly for any power w^n. Inserting into Eq. (4) produces, at leading order, $\dot{R}_0 \propto -R_0^{-1/4}$, which is consistent with Ref. [23] and predicts finite-time blowup of curvature. However, retaining the higher-order terms gives

$$\dot{R}_0 \propto -R_0^{-1/4}\left(1 - \frac{3}{5}\gamma\right), \qquad \gamma(t) = \frac{a_3(t)}{a_1(t)}, \tag{10}$$

which is an exact relation (no truncation). Equation (10) opens the possibility for the curvature divergence to be controlled by the term $(1-(3/5)\gamma)$, and indeed the equilibrium solution Eq. (8) has the property $\gamma = 5/3$.

To further examine this possibility, Fig. 3(c) shows the simulated dissolution of three initial conditions surrounding the equilibrium: $s(w,0) = a_1(0)w + a_3(0)w^3$, with γ initially set to 5/3, 4/3, and 3. The figure confirms that $\gamma = 5/3$ results in nearly constant curvature [45], whereas $\gamma > 5/3$ ($\gamma < 5/3$) leads to decreasing (increasing) curvature, consistent with the sign of $\dot{R}_0$ in Eq. (10). Thus, both tip sharpening and blunting are possible [25,26], with the value of γ determining which occurs. The case $\gamma = 4/3$ leads to tip sharpening, but, due to the proximity to the equilibrium, not nearly as much as in our first numerical example. Thus, the enormous curvature growth observed in Fig. 2 should not always be expected, as it depends on the initial shape.

We now turn attention to the experimentally measured shapes that were shown in Fig. 1, for planar (2D) and axisymmetric (3D) geometries. Figure 4(a) compares the experimental profiles (shifted to have the same apex) to the equilibrium morphology of Eq. (8) (thick gray curve). At late times, the experimental profiles all collapse onto the predicted shape in both two and three dimensions, thus conclusively confirming that Eq. (8) accurately describes the equilibrium spire morphology of a body dissolving under its own solute-induced convective flow. This agreement with laboratory experiments also validates modeling assumptions made, including the boundary-layer and quasisteady approximations and the omission of GT effects.

A second test is made possible by the far-field ($|s| \to \infty$) behavior of the equilibrium solution

$$y \sim \frac{3}{4} R_0^{*-1/3} x^{4/3}, \tag{11}$$

which holds in both two and three dimensions [with $(x,y) \to (r,z)$ in three dimensions, see Supplemental Material [39]]. Figure 4(b) shows a log-scale comparison between this predicted 4/3-power law and the experimental measurements. At late times, the experimental profiles indeed converge to the predicted power law in both cases. We note that this power law is consistent with one of the similarity solutions found in Refs. [25,26], which would need to be asymptotically matched to an inner (near-tip) solution. Those similarity solutions, however, predict

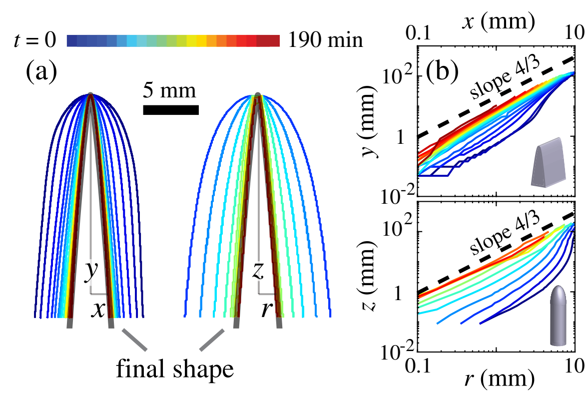

FIG. 4. Comparison with laboratory experiments shown in Fig. 1. (a) When overlaid, the profiles measured from the planar (2D) and axisymmetric (3D) experiments are seen to converge to the shape predicted by Eq. (8). Plotting the experimentally measured surface coordinates on a log-scale confirms the far-field prediction Eq. (11).

continued evolution of shape, whereas we have found convergence to a final form. Numerical and experimental evidence suggests this final morphology to be a stable attractor.

Closer examination of our exact solutions offers an interpretation of the flow-physics underlying the convergence in shape dynamics. Within the boundary layer, a few competing effects exist. First, the apex is in contact with nearly pure liquid, whereas a solute mixture washes over the downstream portions. In isolation, this effect would cause the apex to retreat fastest. On the other hand, the buoyancy-driven flow accelerates as it advances downstream, due to the accumulation of dense solute as well as the increase in surface steepness. This effect enhances convection-induced dissolution on *downstream* portions. Which effect is stronger depends on the detailed geometry of the object, and it is the interplay between the two that drives shape change. Ultimately, balance is achieved by the steadily translating distribution, $V_n = -V_0 \sin\theta$, which shows that the dissolution rate is highest at the tip ($\theta = \pi/2$) and decreases locally in proportion to the surface steepness. At this stage, the mass loss rate of the pinnacle has a simple scaling $dm/dt \sim 2\int_{\theta_0}^{\pi/2} V_n(\theta)R^*(\theta)d\theta \sim -V_0 R_0^* \sim -(R_0^*)^{3/4}$, implying that the mass loss slows as the tip sharpens.

Discussion.—In this Letter, we have described, in exact form, the final spire morphology of a body being reshaped under its own dissolution-induced natural convective flow, thereby concluding the search from Refs. [23–26,38]. Carefully designed numerics show that, rather than forming a geometric shock, characteristics avoid crossing to pursue this terminal shape, which exhibits large, but finite tip curvature. This situation is perhaps analogous to exact solutions found in the context of free surface flows, whose finite curvature reversed previous hypotheses on the formation of cusp singularities [46].

The simple, explicit nature of our solutions suggests that they may be used to infer properties, e.g., age or past environmental conditions, of natural structures. To take one example, suppose that a karst pinnacle at time t_0 has height $h(t_0)$, width $d(t_0)$, and that its apex dissolves at the rate $\dot{h}(t_0) = V(t_0)$. As it nears the final shape, Eq. (11) suggests $h(t)d(t)^{-4/3} = h(t_0)d(t_0)^{-4/3}$ and the constant tip velocity gives $h(t) - h(t_0) = V(t_0)(t - t_0)$. These two relationships comprise a closed system for $[d(t), h(t)]$ at any given time—including the past ($t < t_0$) and the future ($t > t_0$)—thus offering the potential to estimate the past dimensions or, if the dimensions can be estimated through other means, the age of the structure. To take this idea one step further, the typical spacing L between pinnacles in a stone forest approximates the initial width $d(0) \approx L$, thus offering simple estimates for the pinnacle's initial height $h(0) = h(t_0)[L/d(t_0)]^{4/3}$ and its age $t_0 = [h(t_0) - h(0)]/V(t_0)$. Though natural systems involve a range of other complicating factors (such as rainfall, turbulent boundary layers, and fracture) our calculations, based principally on dissolution and fluid dynamics, may offer a leading-order understanding of these amazing structures.

Aspects of our analysis can be extended to other physical systems. For example, Eq. (6) can have a separable solution $R(\theta, t) = A(\theta)B(t)$, corresponding to the self-similar evolution of erodible and soluble bodies immersed in an externally forced flow [1,2,43]. Meanwhile, our approach can be applied to dynamics with an opposite sign in V_n, seen in growing systems like crystallization [44] and the formation of stalactites [16,17].

J. M. H. acknowledges support from the Science and Technology Commission of Shanghai Municipality (Grant 21YF1432100), and the NYU-ECNU Institute of Physics at NYU Shanghai (Challenge Grant). N. M. acknowledges support from the National Science Foundation (Grant DMS-2012560).

J. M. H. and N. J. M. contributed equally to this work.

*machuang@nyu.edu
†nickmoore83@gmail.com

[1] L. Ristroph, M. N. J. Moore, S. Childress, M. J. Shelley, and J. Zhang, Sculpting of an erodible body by flowing water, Proc. Natl. Acad. Sci. U.S.A. **109**, 19606 (2012).
[2] J. M. Huang, M. N. J. Moore, and L. Ristroph, Shape dynamics and scaling laws for a body dissolving in fluid flow, J. Fluid Mech. **765** (2015).
[3] M. M. Sweeting, *Karst in China: Its Geomorphology and Environment* (Springer Science & Business Media, Berlin, 2012), Vol. 15.
[4] D. Ford and P. D. Williams, *Karst Hydrogeology and Geomorphology* (John Wiley & Sons, New York, 2013).
[5] J. A. Whitehead, Moving heaters as a model of continental drift, Phys. Earth Planet. Inter. **5**, 199 (1972).
[6] J. A. Whitehead, Fluid models of geological hotspots, Annu. Rev. Fluid Mech. **20**, 61 (1988).
[7] J.-Q. Zhong and J. Zhang, Thermal convection with a freely moving top boundary, Phys. Fluids **17**, 115105 (2005).
[8] J. M. Huang, J.-Q. Zhong, J. Zhang, and L. Mertz, Stochastic dynamics of fluid–structure interaction in turbulent thermal convection, J. Fluid Mech. **854**, R5 (2018).
[9] P. Meakin and B. Jamtveit, Geological pattern formation by growth and dissolution in aqueous systems, Proc. Math. Phys. Eng. Sci. **466**, 659 (2010).
[10] P. S. Dodds and D. H. Rothman, Scaling, universality, and geomorphology, Annu. Rev. Earth Planet Sci. **28**, 571 (2000).
[11] M. B. Short, J. C. Baygents, and R. E. Goldstein, A free-boundary theory for the shape of the ideal dripping icicle, Phys. Fluids **18**, 083101 (2006).
[12] R. A. Callander, River meandering, Annu. Rev. Fluid Mech. **10**, 129 (1978).
[13] H.-H. Stølum, River meandering as self-organization process, Science **271**, 1710 (1996).
[14] C. A. Braudrick, W. E. Dietrich, G. T. Leverich, and L. S. Sklar, Experimental evidence for the conditions necessary to

sustain meandering in coarse-bedded rivers, Proc. Natl. Acad. Sci. U.S.A. **106**, 16936 (2009).

[15] V. C. Allison, The growth of stalagmites and stalactites, J. Geol. **31**, 106 (1923).

[16] M. B. Short, J. C. Baygents, J. W. Beck, D. A. Stone, R. S. Toomey III, and R. E. Goldstein, Stalactite Growth as a Free-Boundary Problem: A Geometric Law and Its Platonic Ideal, Phys. Rev. Lett. **94**, 018501 (2005).

[17] M. B. Short, J. C. Baygents, and R. E. Goldstein, Stalactite growth as a free-boundary problem, Phys. Fluids **17**, 083101 (2005).

[18] K. Amin, J. Mac Huang, K. J. Hu, J. Zhang, and L. Ristroph, The role of shape-dependent flight stability in the origin of oriented meteorites, Proc. Natl. Acad. Sci. U.S.A. **116**, 16180 (2019).

[19] A. Ginés, M. Knez, T. Slabe, and W. Dreybrodt, *Karst Rock Features. Karren Sculpturing: Karren Sculpturing* (Založba ZRC, Ljubljana, 2009), Vol. 9.

[20] L. H. Song, Origination of stone forests in China, Int. J. Speleol. **15**, 1 (1986).

[21] M. Veress, D. Lóczy, Z. Zentai, G. Tóth, and R. Schläffer, The origin of the Bemaraha tsingy (Madagascar), Int. J. Speleol. **37**, 6 (2008).

[22] T. Slabe, A. Hada, and M. Knez, Laboratory modeling of karst phenomena and their rock relief on plaster: Subsoil karren, rain flutes karren and caves, Acta carsologica **45** (2016).

[23] J. M. Huang, J. Tong, M. Shelley, and L. Ristroph, Ultra-sharp pinnacles sculpted by natural convective dissolution, Proc. Natl. Acad. Sci. U.S.A. **117**, 23339 (2020).

[24] E. Nakouzi, R. E. Goldstein, and O. Steinbock, Do dissolving objects converge to a universal shape? Langmuir **31**, 4145 (2014).

[25] S. S. Pegler and M. S. D. Wykes, Shaping of melting and dissolving solids under natural convection, J. Fluid Mech. **900**, A35 (2020).

[26] S. S. Pegler and M. S. D. Wykes, The convective Stefan problem: shaping under natural convection, J. Fluid Mech. **915**, A86 (2021).

[27] H. B. Aaron and G. R. Kotler, The effects of curvature on the dissolution kinetics of spherical precipitates, Metal science Journal **4**, 222 (1970).

[28] M. Perez, Gibbs–Thomson effects in phase transformations, Scr. Mater. **52**, 709 (2005).

[29] M. N. J. Moore, Riemann-Hilbert problems for the shapes formed by bodies dissolving, melting, and eroding in fluid flows, Commun. Pure Appl. Math. **70**, 1810 (2017).

[30] J. M. Huang, M. J. Shelley, and D. B. Stein, A stable and accurate scheme for solving the Stefan problem coupled with natural convection using the Immersed Boundary Smooth Extension method, J. Comput. Phys. **432**, 110162 (2021).

[31] C. H. Rycroft and M. Z. Bazant, Asymmetric collapse by dissolution or melting in a uniform flow, Proc. Math. Phys. Eng. Sci. **472**, 20150531 (2016).

[32] W. H. Mitchell and S. E. Spagnolie, A generalized traction integral equation for Stokes flow, with applications to near-wall particle mobility and viscous erosion, J. Comput. Phys. **333**, 462 (2017).

[33] J. N. Hewett and M. Sellier, Evolution of an eroding cylinder in single and lattice arrangements, J. Fluids Struct. **70**, 295 (2017).

[34] N. J. Derr, D. C. Fronk, C. A. Weber, A. Mahadevan, C. H. Rycroft, and L. Mahadevan, Flow-Driven Branching in a Frangible Porous Medium, Phys. Rev. Lett. **125**, 158002 (2020).

[35] B. D. Quaife and M. N. J. Moore, A boundary-integral framework to simulate viscous erosion of a porous medium, J. Comput. Phys. **375**, 1 (2018).

[36] S.-H. Chiu, M. N. J. Moore, and B. Quaife, Viscous transport in eroding porous media, J. Fluid Mech. **893** (2020).

[37] A. J. C. Ladd, L. Yu, and P. Szymczak, Dissolution of a cylindrical disk in Hele-Shaw flow: A conformal-mapping approach, J. Fluid Mech. **903** (2020).

[38] M. S. Davies Wykes, J. M. Huang, G. A. Hajjar, and L. Ristroph, Self-sculpting of a dissolvable body due to gravitational convection, Phys. Rev. Fluids **3**, 043801 (2018).

[39] See Supplemental Material at http://link.aps.org/supplemental/10.1103/PhysRevLett.128.024501 for boundary layer model, numerical implementation, and exact solutions for the final shape.

[40] H. Schlichting and K. Gersten, *Boundary-Layer Theory* (Springer, New York, 2016).

[41] T. Y. Hou, J. S. Lowengrub, and M. J. Shelley, Removing the stiffness from interfacial flows with surface tension, J. Comput. Phys. **114**, 312 (1994).

[42] S. Alben, M. Shelley, and J. Zhang, Drag reduction through self-similar bending of a flexible body, Nature (London) **420**, 479 (2002).

[43] M. N. J. Moore, L. Ristroph, S. Childress, J. Zhang, and M. J. Shelley, Self-similar evolution of a body eroding in a fluid flow, Phys. Fluids **25**, 116602 (2013).

[44] J. S. Wettlaufer, M. Jackson, and M. Elbaum, A geometric model for anisotropic crystal growth, J. Phys. A **27**, 5957 (1994).

[45] The curvature does not remain exactly constant due to the fact that this initial condition is not the terminal shape from Eq. (8), but a truncation of it.

[46] J.-T. Jeong and H. Moffatt, Free-surface cusps associated with flow at low Reynolds number, J. Fluid Mech. **241**, 1 (1992).